

# Terahertz binding of nanoparticles based on graphene surface plasmons excitations

Hernan Ferrari<sup>a,b</sup>, Carlos J. Zapata-Rodríguez<sup>c</sup>, Mauro Cuevas<sup>a,b,\*</sup>

<sup>a</sup>Consejo Nacional de Investigaciones Científicas y Técnicas (CONICET).

<sup>b</sup>Facultad de Ingeniería, Universidad Austral, Mariano Acosta 1611, Pilar 1629, Buenos Aires, Argentina.

<sup>c</sup>Department of Optics and Optometry and Vision Sciences, University of Valencia, Dr. Moliner 50, 46100, Burjassot, Spain.

## Abstract

This work studies the optical binding of a dimer composed by dielectric particles close to a graphene sheet. Using a rigorous electromagnetic method, we calculated the optical force acting on each nanoparticle. In addition, we deduced analytical expressions enabling to evaluate the contribution of graphene surface plasmons (GSPs) to optical binding. Our results show that surface plasmon on graphene excitations generate multiple equilibrium positions for which the distance between particles are tens of times smaller than the photon wavelength. Moreover, these positions can be dynamically controlled by adjusting the chemical potential on graphene. Normal and oblique incidence have been considered.

**Keywords:** surface plasmon, graphene, THz nanoparticles binding

**PACS:** 81.05.ue, 73.20.Mf, 78.68.+m, 42.25.Fx

## 1. Introduction

The scattered field by a neutral particle assembly can result, under particular conditions, in an effective dipole–dipole interaction useful for optically binding the particle array. Most of the literature in this field has been devoted to micro–sized particles, since the significant electromagnetic scattering at this scale makes the strength of optical binding surpassing the hydrodynamic interactions and the stochastic thermal activation [1, 2].

The significant progress made in experimental techniques and the extensive wealth of theoretical research have meet the need of optical binding between nano sized particles. In this context, the effect of localized surface plasmon excitations on assembly clusters of metallic nanoparticles has been theoretically and experimentally demonstrated [3, 4, 5, 6]. In addition, stable optical binding between dielectric nano particles using an evanescent field formed by total reflection at a dielectric interface has been demonstrated [7, 8]. Recently, a planar metallic or metamaterial structure was proposed as an optical binding tool, in which the propagating eigenmodes excited on the surface play an essential role on the increment of the interaction force between dielectric nano particles. The binding distance between nanoparticles is defined by the eigenmode wavelength which, in case of bound modes such as surface plasmons, is smaller than the photon wavelength [9, 10].

It is known, apart from the well known surface plasmons supported by a metallic surface, long livid propagating plasmons can be supported by graphene from terahertz (THz) to infrared (IR) frequency range. GSPs present good tunability through

electrical or chemical modification of the carrier density, relative low loss and tightly confined fields. These properties have been the subject of theoretical and experimental studies to find application in a wide range of disciplines. For example, GSPs have been proposed as a new generation of nano antennas for communications in the THz bands [11], molecular sensors capable to selectively enhance individual spectral features [12, 13], low frequency spaser (see [14] and Refs. therein) and for enhancing the spontaneous emission and energy transfer between molecules [15, 16, 17]. Recently, the use of high-quality GSP resonances on twin graphene–coated dielectric rods to enhance the diffraction radiation intensity in the IR region has been demonstrated [18].

Regarding to optical tweezers framework, some works have focused on the optical trapping using graphene as plasmonic material [19, 20]. In these structures, GSPs provided the channels for capturing a small dielectric nanoparticle [21] or trapping and sorting nanoparticles [22]. In [23], authors proposed a nanopatterned graphene structure for particle trapping/levitation. In addition, optical force on the nonlinear graphene–wrapped nanoparticle has been investigated [24].

A natural question that arises from the above outstanding characteristics is whether propagating GSPs can be useful for binding particles, taking advantage of their great localization to bind particles greatly exceeding the diffraction limit. In particular, how GSPs enable dielectric nanoparticles to be bound at distances of few hundred nanometers between them by using low frequency radiation instead of visible radiation. In consequence, the present work is theoretically developed in order to respond to these questions. Specifically, we analytically study the binding conditions for a dimer formed by dielectric nanoparticles, providing a complete description about the use of GSPs to create equilibrium positions solely by plane wave

\*corresponding author

Email address: mcuevas@austral.edu.ar (Mauro Cuevas)

radiation. Since the kinematic properties of GSPs can be controlled by chemical potential variations, possibilities to dynamically control the equilibrium positions without changing the geometrical parameters of the structure are opened.

This paper is organized as follows. In section 2, we present a brief description of the analytical method, based on the Green approach, to calculate the optical force between two dielectric nanoparticles placed above a graphene sheet. By using contour integration in the complex plane, we obtained simple formulas, which contain the GSP contribution to the optical force, that reproduce the main results obtained by applying the rigorous theory. In section 3, we exemplify for both normally and obliquely incident illumination cases, and for different particle shapes. Concluding remarks are provided in section 4. The international system of units is used and an  $\exp(-i\omega t)$  time-dependence is implicit throughout the paper, where  $\omega$  is the angular frequency,  $t$  is the time coordinate, and  $i = \sqrt{-1}$ . The symbols Re and Im are used for denoting the real and imaginary parts of a complex quantity, respectively.

## 2. Theory

### 2.1. Optical binding.

We consider a system formed by two dielectric particles placed above of a plane graphene sheet (at  $z = 0$ ) separating two homogeneous half spaces, vacuum ( $\varepsilon_1 = 1$ ) and a non-magnetic and isotropic dielectric medium ( $\varepsilon_2 = 2.13$ ). Both dielectric particles are identical. Spherical particles are characterized by radius  $R_1 = R_2 = R$ , and other shapes are taken in such a way the volumes of these objects are equal to that of the sphere. The relative permittivity of the particles is  $\varepsilon_p$  and they are placed at  $\mathbf{r}_A = z_0\hat{z}$  and  $\mathbf{r}_B = x_0\hat{x} + z_0\hat{z}$  ( $z_0 \geq 0$ ) in the field of an incident plane wave (see Fig. 1).

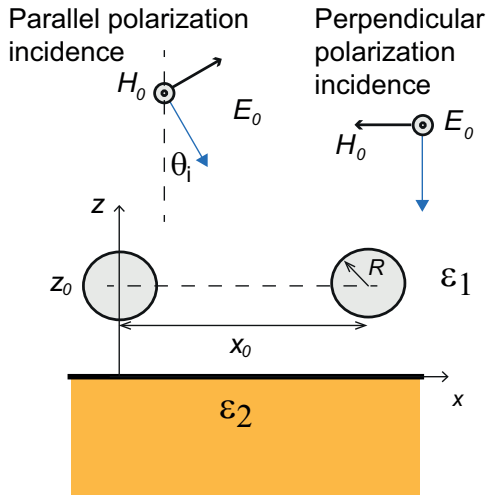


Figure 1: Schematic of the problem. Two identical particles of permittivity  $\varepsilon_p$  under illumination of a plane wave. The particles are embedded in vacuum ( $\varepsilon_1 = 1$ ) at a distance  $z_0$  from the graphene plane, at  $z = 0$ , that separates the vacuum from a dielectric medium characterized by a permittivity  $\varepsilon_2 = 2.13$ . In case of normal incidence, the electric field can be parallel (parallel polarization) or perpendicular (perpendicular polarization) to the axis joining the particles.

Taking into account that the size of the particles are smaller than plasmon and photon wavelengths ( $R < \lambda_{sp} \ll \lambda$ ), we can use the dipolar approximation. In this framework, the time average of the total force acting on a single particle is [26],

$$\mathbf{F}(\mathbf{r}) = \frac{1}{2} \text{Re} \sum_{j=x,y,z} p_j^* \nabla E_j(\mathbf{r}), \quad (1)$$

where  $E_j$  is the  $j$  component of the electric field,  $\mathbf{p} = \alpha_0 \mathbf{E}$  is the induced electric dipole on particle at  $\mathbf{r}$  position,

$$\alpha_0 = \frac{\alpha_e}{1 - i \frac{k_0^3}{6\pi\varepsilon_0} \alpha_e}, \quad (2)$$

is the radiation corrected electric polarizability,  $k_0 = 2\pi/\lambda$  is the modulus of the vacuum photon wavevector,  $\varepsilon_0$  is the vacuum permittivity and  $\alpha_e$  is the electrostatic approximation of particle polarizability. In case of spherical particle,

$$\alpha_e = 4\pi\varepsilon_0 R^3 \frac{\varepsilon_p - \varepsilon_1}{\varepsilon_p + 2\varepsilon_1}. \quad (3)$$

In case of other shapes such as cubes or cylinders particles, we have calculated the  $\alpha_e$  polarizability following the accurate formulas presented in [27].

The electric field in Eq. (1) is given by

$$\mathbf{E}(\mathbf{r}) = \mathbf{E}_0 + \frac{k_0^2}{\varepsilon_0} \hat{\mathbf{G}}(\mathbf{r}, \mathbf{r}_A) \mathbf{p}_A + \frac{k_0^2}{\varepsilon_0} \hat{\mathbf{G}}(\mathbf{r}, \mathbf{r}_B) \mathbf{p}_B, \quad (4)$$

where  $\mathbf{E}_0$  is the superposition of the incident field and the reflected field on the flat substrate,  $\hat{\mathbf{G}}(\mathbf{r}, \mathbf{r}_j) = \hat{\mathbf{G}}_0(\mathbf{r}, \mathbf{r}_j) + \hat{\mathbf{G}}_s(\mathbf{r}, \mathbf{r}_j)$  is the sum of the vacuum and the scattered-by-the-surface Green tensors of a point dipole. Second and third terms in Eq. (4) correspond to the scattered electric fields on  $\mathbf{r}$  position by the electric dipole in particle A and B, respectively. By solving the self consistent Eq. (4) for  $\mathbf{E}(\mathbf{r}_j)$  ( $j = A, B$ ) and using Eq. (1) we can calculate the optical force on particle A or B. An equivalent form using the effective particle polarizabilities defined in Appendix C that simplify the force calculation was considered in [3, 9]. For example, by using the expression for  $\mathbf{p}_A$  given by Eq. (D4) and that equivalent for  $\mathbf{p}_B$ , Eqs. (4) and Eq. (1), we obtain an expression for the force on particle B,

$$\mathbf{F}(\mathbf{r}_B) = \frac{1}{2} \text{Re} \sum_{j=x,y,z} p_{Bj}^* \nabla E_j(\mathbf{r})|_{\mathbf{r}_B} = \frac{1}{2} \text{Re} \sum_{j=x,y,z} p_{Bj}^* \nabla \left\{ [\mathbf{E}_0(\mathbf{r})]_j + \frac{k_0^2}{\varepsilon_0} [\hat{\mathbf{G}}(\mathbf{r}, \mathbf{r}_A) \mathbf{p}_A]_j + \frac{k_0^2}{\varepsilon_0} [\hat{\mathbf{G}}(\mathbf{r}, \mathbf{r}_B) \mathbf{p}_B]_j \right\} |_{\mathbf{r}_B}, \quad (5)$$

where  $[\cdot]_j$  indicates the  $j$  coordinate of  $\cdot$ . An equivalent equation can be obtained for particle A.

### 2.2. Graphene surface plasmon contribution.

Graphene surface plasmons, eigenmodes of the structure that propagate along the graphene surface with their electric and magnetic fields decaying exponentially away from the graphene sheet, can provide channels for enhancing the optical force between particles. Since  $\text{Im } \sigma > 0$  ( $\sigma$  is the graphene conductivity) in the frequency range considered in this work, only  $p$  polarized GSPs exist, *i.e.*, surface waves with the total magnetic

field parallel to the surface [28]. Thus, the full characteristics of the GSPs can be obtained by studying the singularities of the analytic continuation of the reflection coefficient  $r_p(k_{\parallel})$ . Pole singularities occur at complex locations and they represent the propagation constant  $k_{sp}$  of the GSPs. Since the integration path in Green's functions

$$\hat{\mathbf{G}}_s(\mathbf{r}_B, \mathbf{r}_A) = \frac{i}{8\pi^2} \int_0^{\infty} dk_{\parallel} \mathbf{f}(k_{\parallel}, \rho) e^{i\gamma^{(1)}(z_A+z_B)}, \quad (6)$$

is set along the real and positive  $k_{\parallel}$  axis, the integral, and consequently the Green's functions, will be strongly affected by singularities  $k_{\parallel} = k_{sp}$  that are close to that axis. In Eq. (6),  $k_{\parallel}$  is the wave vector parallel to the surface,  $\rho = \sqrt{|\mathbf{r}_A - \mathbf{r}_B|^2 - (z_A - z_B)^2}$  and functions  $\mathbf{f}(k_{\parallel}, \rho)$  are defined in Appendix B. Following the same steps as in Ref. [25], we can extract the GSP contribution from the Green functions  $\mathbf{G}_s(\mathbf{r}, \mathbf{r}_j)$  ( $j = A, B$ ) as follows. Since the procedure is similar for all components of  $\hat{\mathbf{G}}_s(\mathbf{r}, \mathbf{r}')$ , we show it for the  $xx$  component. Applying the symmetry properties of Bessel integrals [25],

$$\begin{aligned} \int_0^{+\infty} f_{odd}(x) J_0(x) dx &= \frac{1}{2} \int_{-\infty}^{+\infty} f_{odd}(x) H_0^{(1)}(x) dx, \\ \int_0^{+\infty} f_{even}(x) J_1(x) dx &= \frac{1}{2} \int_{-\infty}^{+\infty} f_{even}(x) H_1^{(1)}(x) dx, \end{aligned} \quad (7)$$

where  $f_{odd}(x)$  and  $f_{even}(x)$  are odd and even functions, respectively, of the argument, we obtain

$$\begin{aligned} \hat{G}_{s,xx}(\mathbf{r}_B, \mathbf{r}_A) &= \frac{i}{8\pi^2} \int_{-\infty}^{\infty} dk_{\parallel} 2\pi \\ &\times \frac{k_{\parallel} \gamma^{(1)}}{k_0^2} \frac{1}{2} \left[ \frac{H_1(k_{\parallel} x_0)}{k_{\parallel} x_0} - H_0(k_{\parallel} x_0) \right] r_p(k_{\parallel}) e^{i2\gamma^{(1)} z_0} = \\ &- \frac{i}{8\pi^2} \int_{-\infty}^{\infty} dk_{\parallel} 2\pi \frac{k_{\parallel} \gamma^{(1)}}{k_0^2} \frac{1}{2} H_1'(k_{\parallel} x_0) r_p(k_{\parallel}) e^{i2\gamma^{(1)} z_0}, \end{aligned} \quad (8)$$

where we only have considered the  $p$  polarization. In the last equality in Eq. (8) we used the fact that  $H_1(z)/z - H_0(z) = -H_1'(z)$ . Note that we have set  $\theta = 0$ ,  $z_A = z_B = z_0$  and  $\rho = x_0$  to write Eq. (8) because both particles are on  $x$  axis and at the same distance from the graphene plane. We now deform the integration path in (8) into a semicircle of large radius ( $|k_{\parallel}| \rightarrow \infty$ ) in the positive imaginary half-plane  $\text{Im}k_{\parallel} > 0$ , avoiding the branch point and pole singularities, as in Ref. [25]. Then, the residues theorem gives

$$\hat{G}_{s,xx}(\mathbf{r}_B, \mathbf{r}_A) = \frac{k_{sp} \gamma_{sp}^{(1)}}{4k_0^2} H_1'(k_{sp} x_0) e^{i2\gamma_{sp}^{(1)} z_0} \text{Res } r_p, \quad (9)$$

where  $k_{sp}$  is the propagation constant of GSPs,  $\gamma^{(1)} = \sqrt{k_0^2 - k_{sp}^2}$  and

$$\text{Res } r_p = \lim_{k_{\parallel} \rightarrow k_{sp}} (k_{\parallel} - k_{sp}) r_p. \quad (10)$$

As  $k_{sp}$  is almost real and higher than the modulus of the photon wave vector  $k_0$ ,  $\gamma^{(1)} \approx i\gamma_{sp}$  with  $\gamma_{sp} = \sqrt{k_{sp}^2 - k_0^2}$  a real number ( $k_{sp} > k_0$ ). Thus, Eq. (9) can be written as,

$$\hat{G}_{s,xx}(\mathbf{r}_B, \mathbf{r}_A) = i \frac{k_{sp} \gamma_{sp}}{4k_0^2} H_1'(k_{sp} x_0) e^{-2\gamma_{sp} z_0} \text{Res } r_p. \quad (11)$$

Using the non retarded approximation, *i.e.*,  $k_0 \ll k_{sp}$ , it follows  $\gamma_{sp} = k_{sp}$  and  $\text{Res } r_p = 2k_{sp}/(\varepsilon_1 + \varepsilon_2)$  (see Appendix D). As a consequence, Eq. (11) takes the form,

$$\hat{G}_{s,xx}(\mathbf{r}_B, \mathbf{r}_A) = i \frac{k_{sp}^3}{2k_0^2(\varepsilon_1 + \varepsilon_2)} H_1'(k_{sp} x_0) e^{-2k_{sp} z_0}. \quad (12)$$

Taking the limit case for  $\mathbf{r}_A$  tending to  $\mathbf{r}_B$ , we obtain

$$\hat{G}_{s,xx}(\mathbf{r}_B, \mathbf{r}_B) = i \frac{k_{sp}^3}{4k_0^2(\varepsilon_1 + \varepsilon_2)} e^{-2k_{sp} z_0}. \quad (13)$$

Now, we can use Eq. (5) to calculate the force in the  $x$  direction.

Firstly, we begin by studying the case of normal incidence. In the limit case in which the diagonal elements of the effective polarizability tensor (D7) are dominant [9], from Eq. (5), the  $x$  component of the optical force on particle B can be approximated by,

$$F_x^{(GSP,x)}(\mathbf{r}_B) = \frac{1}{2} \frac{k_0^2}{\varepsilon_0} \left\{ \text{Re } p_{Bx}^* \frac{\partial}{\partial x} [\hat{G}_{s,xx}(\mathbf{r}, \mathbf{r}_A)]|_{\mathbf{r}_B} p_{Ax} + \text{Re } p_{Bx}^* \frac{\partial}{\partial x} [\hat{G}_{s,xx}(\mathbf{r}, \mathbf{r}_B)]|_{\mathbf{r}_B} p_{Bx} \right\}, \quad (14)$$

for the case in which the incident electric field is along the  $x$  axis, and

$$F_x^{(GSP,y)}(\mathbf{r}_B) = \frac{1}{2} \frac{k_0^2}{\varepsilon_0} \left\{ \text{Re } p_{By}^* \frac{\partial}{\partial x} [\hat{G}_{s,yy}(\mathbf{r}, \mathbf{r}_A)]|_{\mathbf{r}_B} p_{Ay} + \text{Re } p_{By}^* \frac{\partial}{\partial x} [\hat{G}_{s,yy}(\mathbf{r}, \mathbf{r}_B)]|_{\mathbf{r}_B} p_{By} \right\}, \quad (15)$$

for the case in which the incident electric field is along the  $y$  axis. Note that we have included the superscript  $x$  and  $y$  in Eqs. (14) and (15) to indicate the direction of the incident electric field. Since,  $\hat{G}_{s,xx}(\mathbf{r}', \mathbf{r}')$  given by Eq. (13) is imaginary, it is follows that  $\frac{\partial}{\partial x} \hat{G}_{s,xx}(\mathbf{r}', \mathbf{r}')$  is imaginary, consequently the last term in Eqs. (14) and (15) does not contribute to the force. Taking derivative respect to  $x$  variable, and considering  $p_{Ax} = p_{Bx} = p_x$  (the field is normally incident on the surface), Eq. (14) is written as

$$F_x^{(GSP,x)}(\mathbf{r}_B) = \text{Re} \left\{ i \frac{1}{2} \frac{k_0^2}{\varepsilon_0} |p_x|^2 \frac{k_{sp}^4}{2k_0^2(\varepsilon_1 + \varepsilon_2)} H_1''(k_{sp} x_0) e^{-2k_{sp} z_0} \right\} \approx \frac{1}{4\varepsilon_0} |p_x|^2 \frac{k_{sp}^4}{(\varepsilon_1 + \varepsilon_2)} Y_1(k_{sp} x_0) e^{-2k_{sp} z_0}. \quad (16)$$

In the last equality we have given the plasmonic force for large range distances,  $x_0 \gg 1/k_{sp}$ . Following the same steps for obtaining Eq. (16), from Eqs. (15) and (B5) with  $\theta = 0$ , we obtain

$$F_x^{(GSP,y)}(\mathbf{r}_B) \approx \frac{1}{4\varepsilon_0} |p_y|^2 \frac{k_{sp}^4}{(\varepsilon_1 + \varepsilon_2)} \frac{Y_2(k_{sp} x_0)}{k_{sp} x_0} e^{-2k_{sp} z_0}, \quad (17)$$

where we have used  $\frac{d}{dx}(H_1(x)/x) = -H_2(x)/x$ . Equations (16) and (17) give the GSP optical force in  $x$  direction between two particles aligned along the  $x$  axis, when the field is normally

incident with its electric field parallel to the  $x$  axis (Eq. (16)) and parallel to the  $y$  axis (Eq. (17)).

Next, we obtain the plasmon contribution for oblique incidence in the case for which the plane of incidence coincides with the  $x$ - $z$  plane. To do this, by following the same procedure as that used to obtain Eq. (12), we extract the GSP contribution from all components of the Green tensor (6) and replace these into Eq. (5),

$$F_x(\mathbf{r}_B) \approx \frac{1}{2} \text{Re} \left\{ ik_0 \sin \theta_i [p_{B_x}^* E_{0x}(\mathbf{r}_B) + p_{B_z}^* E_{0z}(\mathbf{r}_B)] \right. \\ \left. + \frac{k_{sp}^4}{4\epsilon_0(\epsilon_1 + \epsilon_2)} \left( -iH_1(k_{sp}x_0)[p_{B_x}^* p_{Ax} + p_{B_z}^* p_{Az}] \right. \right. \\ \left. \left. -iH_1'(k_{sp}x_0)[p_{B_z}^* p_{Ax} - p_{B_x}^* p_{Az}] + \frac{i}{2}[p_{B_z}^* p_{Bx} - p_{B_x}^* p_{Bz}] \right) \right\} \\ \times e^{-2k_{sp}z_0}, \quad (18)$$

where we have used that  $\hat{G}_{s,xy}(\mathbf{r}_B, \mathbf{r}_A) = \hat{G}_{s,yz}(\mathbf{r}_B, \mathbf{r}_A) = 0$  because  $\theta = 0$  or  $\pi$  in Eqs. (B7) and (B9) (see Appendix B). The first term in Eq. (18) corresponds to the component force along the  $x$  axis of the incident and reflected by the graphene plane surface fields,  $E_{0x}(\mathbf{r}_B) = E_i \cos \theta_i [e^{-ik_0 \cos \theta_i z_0} - r_p e^{ik_0 \cos \theta_i z_0}] e^{ik_0 \sin \theta_i x_B}$  and  $E_{0z}(\mathbf{r}_B) = E_i \sin \theta_i [e^{-ik_0 \cos \theta_i z_0} + r_p e^{ik_0 \cos \theta_i z_0}] e^{ik_0 \sin \theta_i x_B}$ . The second term represents the interaction between two dipole moments, both oriented in the  $x$  and  $z$  axis, respectively, via surface plasmon excitations. The third term represents the interaction between dipole  $A$  and  $B$ , one of them is along the  $x$  axis and the other is along the  $z$  axis, and the last term represents the interaction between both components,  $x$  and  $z$ , of the same dipole moment. The force on particle  $A$  can be obtained from Eq. (18) by permuting the indices  $A$  and  $B$  and changing the sign of function  $H_1(k_{sp}x_0)$  in the second term.

### 3. Results.

In this section, we apply the sketch developed in above sections to calculate the optical force between particles under plane wave illumination. Firstly, our calculations are made for spherical particles and then we take care of others shapes different to spherical ones, like cylinders and cubes. The relative permittivity of the particles are  $\epsilon_p = 3.9$ . The radius of the spheres is  $R = 90\text{nm}$  and the size of cubes and cylinders are taken in such a way the volumes of these three objects are equal. We use the large doping condition for which the graphene conductivity takes a Drude behaviour (see Appendix A). We have normalized the optical force  $F$  with respect to the incident density of power  $I = |E_0|^2/(2Z_0)$ ,  $Z_0 = \sqrt{\mu_0/\epsilon_0}$  is the vacuum impedance, *i.e.*, we calculated  $f = F/I$ , where  $F$  is given in pico-Newton ( $\text{pN}$ ) and  $I$  is given in  $\text{mW}/\mu\text{m}^2$ .

In all the cases, the optical force has been rigorously calculated. To do this, the Green tensor components are calculated following the same procedure as one applied in Ref. [25] (see Appendix E).

Figures 2a and 2b show the optical force for normal incidence as a function of the interparticle distance  $x_0$ , rigorously

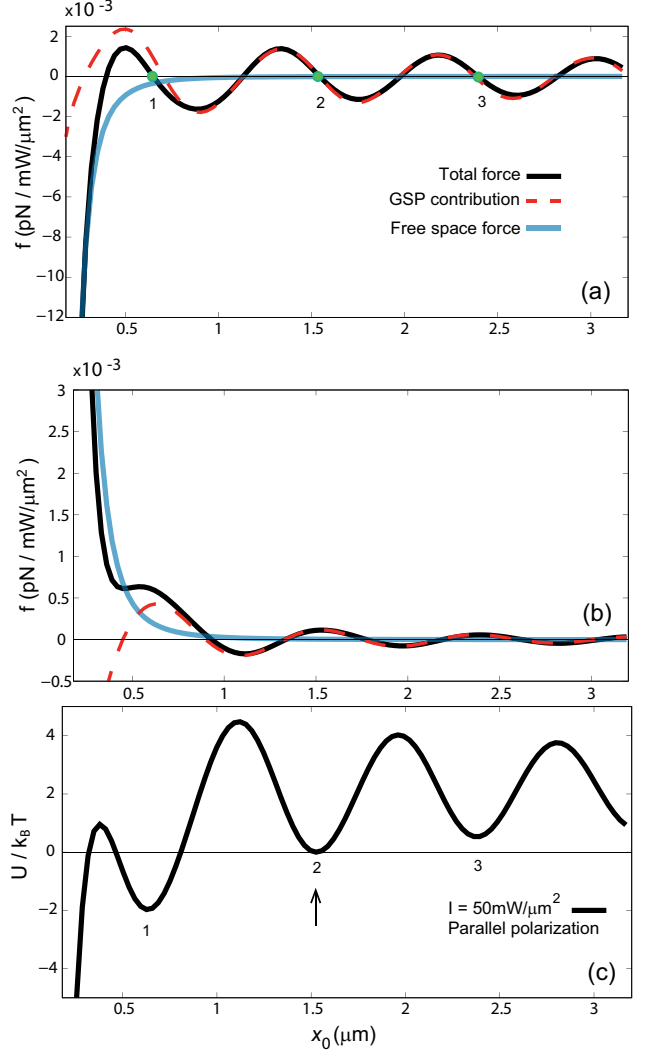


Figure 2: Optical force as a function of the interparticle distance  $x_0$  for (a) parallel and (b) perpendicular polarizations, and (c) potential energy binding normalized to  $k_B T$  for parallel polarization. The potential energy values have been calculated for an intensity  $I = 50 \text{mW}/\mu\text{m}^2$ . The arrow in (c) indicates the position of zero potential, which coincides with the equilibrium position 2. The frequency  $\omega/c = 0.325 \mu\text{m}^{-1}$ , the particle radius  $R = 90 \text{nm}$  and the distance  $z_0 = 100 \text{nm}$ . The graphene parameters are  $\mu_g = 0.3 \text{eV}$  and  $\gamma_g = 0.1 \text{meV}$ .

calculated using Eq. (5), for illumination parallel (electric field parallel to the incidence plane,  $E_i = E_{\parallel}$ ) and perpendicular (electric field perpendicular to the incidence plane,  $E_i = E_{\perp}$ ), respectively, rigorously calculated using Eq. (5). The chemical potential of graphene and frequency are  $\mu_g = 0.3\text{meV}$  and  $\omega/c = 0.325\mu\text{m}^{-1}$  (wavelength  $\lambda = 19.3\mu\text{m}$ ), respectively. In both cases, we observe that the force periodically varies with the  $x_0$  coordinate with a period  $\approx 0.8\mu\text{m}$ . At the incident field frequency, the real part of the calculated GSP propagation constant is  $\text{Re } k_{sp} = 7.55\mu\text{m}^{-1}$ , corresponding to a plasmon wavelength  $\lambda_{sp} = 0.83\mu\text{m}$  which agrees well with the numerically calculated period of the force.

To gain insight about the role of GSPs in the interparticle force, in Figure 2 we plotted the plasmon contributions given by Eqs. (16) and (17). We observe that for  $x_0 > 1\mu\text{m}$  these curves match with those rigorously calculated with Eq. (5), indicating that for interparticle distance values large enough, surface plasmon excitations dominate the optical binding calculated in Figure 2. On the contrary, for small values of  $x_0$  ( $x_0 < 1\mu\text{m}$ ), the surface plasmon contribution departs from the total optical force which is very approximately equal to the one in free space, *i.e.*, to the optical force in absence of graphene. In fact, in this range, the force is attractive when the particles are illuminated with parallel polarization, whereas it is repulsive when particles are illuminated with perpendicular polarization. Moreover, in this range the optical force changes rapidly with  $x_0$ .

All these characteristics can be understood by comparing the contributions of free space and GSP modes in the short distance range between particles.

$$F_x^{(FS)} \approx \frac{1}{2} \frac{k_0^2}{\epsilon_0} \text{Re} \left\{ |p_j|^2 \frac{\partial}{\partial x_j} G_{0,x_j x_j}(\mathbf{r}', \mathbf{r}) \right\}, \quad (19)$$

where  $j = x$  for parallel polarization and  $j = y$  for perpendicular polarization,  $G_{0,xx}$  and  $G_{0,yy}$  are the components of free Green tensor (Eq. (B12)),  $\mathbf{r} = x_0\hat{x} + z_0\hat{z}$  and  $\mathbf{r}' = z_0\hat{z}$ . Taking the derivative of  $G_{0,xx}$  and  $G_{0,yy}$  components of free Green tensor (Eq. (B12)), we obtain,  $F_x^{(FS)} \approx -|p_x|^2/x_0^4$  for parallel polarization and  $F_x^{(FS)} \approx |p_y|^2/x_0^4$  for perpendicular polarization. The negative sign indicates that the force is attractive for parallel polarization, whereas the positive sign corresponds to a repulsive force for perpendicular polarization. This is consistent with the intuitive idea that in this range, where the plasmonic contribution can be neglected, the polarization charges on the surface of particles are asymmetric for parallel polarization, resulting in an attractive force. On the contrary, for perpendicular polarization the surface charge distribution on particles is symmetric, resulting in a repulsive force [5]. While the spatial dependence of the free space contribution is  $\approx \pm 1/x_0^4$ , the GSP contribution given by Eqs. (16) and (17) is  $F_x^{(GSP)} \approx 1/x_0^3$ . From the above analysis, we conclude that free space contributions dominate the optical force interaction at short distances.

In Figure 2a we have plotted points at stable positions, these are, points on the  $x_0$  axis where the optical force pass from positive to negative values [9]. In this range, the normalized total

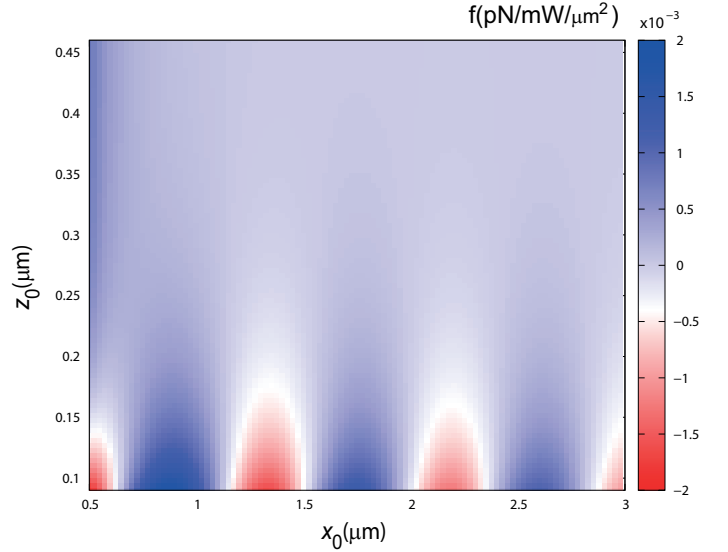


Figure 3: Map of the optical force as a function of the interparticle distance  $x_0$  and the height  $z_0$  for  $\omega/c = 0.325\mu\text{m}^{-1}$  and  $\mu_g = 0.3\text{eV}$ . All other parameters are the same as in Figure 2.

force reaches a value  $\approx 1.4 \times 10^{-3} \text{pN}$ , *i.e.*, a value of  $0.07 \text{pN}$  for intensities of  $50 \text{mW}/\mu\text{m}^2$ . Taking into account that the period of the force is  $\lambda_p = 0.83\mu\text{m}$ , the trapping potential of the optical binding approaches  $4k_B T$  at room temperature and moderate intensities involved in optical trapping [9, 10]. This fact can be seen in Figure 2c, where we have calculated the potential energy of the optical binding for parallel polarization by integration of the force for an intensity of  $50 \text{mW}/\mu\text{m}^2$  (we take the potential energy as null for the equilibrium position 2). To do this, we used the fact that the particles are smaller than the wavelength, which results in low values of the imaginary part of the polarizability  $\hat{\alpha}_j$  ( $j = A, B$ ) and, consequently, the non conservative part of the force (radiation force) can be neglected [9, 29]. On the other hand, note that stable first positions are at  $x_0 \approx 1.5\mu\text{m}$ , a value near 15 times lower than that corresponding to the free space, which falls at  $x_0 \approx 22\mu\text{m}$  [not shown in Figure 2], which demonstrates the high subwavelength binding that is provided by GSPs.

By comparing Figures 2a and 2b, we observe that for  $x > 1\mu\text{m}$ , the force values for perpendicular polarization are one order of magnitude less than those for parallel polarization. This is because, in this range, where the force is dominated by the plasmon contribution, the optical force for perpendicular polarization decays faster than that corresponding to parallel polarization ( $F_x^{(y)} \approx Y_2(k_{sp}x_0)/(k_{sp}x_0)$  and  $F_x^{(x)} \approx Y_1(k_{sp}x_0)$ ). As a consequence, the stable trapping for moderate intensity, with the parameters considered here, is then impossible for perpendicular polarization.

In what follows, we only present calculations for parallel polarization.

In Figure 3 we calculated the optical force for normal incidence as a function of  $x_0$  and  $z_0$  for  $\mu_g = 0.3\text{eV}$  and  $\omega/c = 0.325\mu\text{m}^{-1}$ . We see that the force presents the same periodic behaviour, with respect  $x_0$  variable, as in Figure 2, passing from

positive to negative values with the period of the plasmon wavelength  $\lambda_{sp} = 0.83\mu\text{m}$ . In addition, the force values quickly decrease with the height  $z_0$  and practically disappear for  $z_0$  values larger than  $0.35\mu\text{m}$ . This can be understood from Eqs. (16) and (17), where we observe an exponential decay of the force with  $z_0$  as  $\approx \exp(-2k_{sp}z_0)$ .

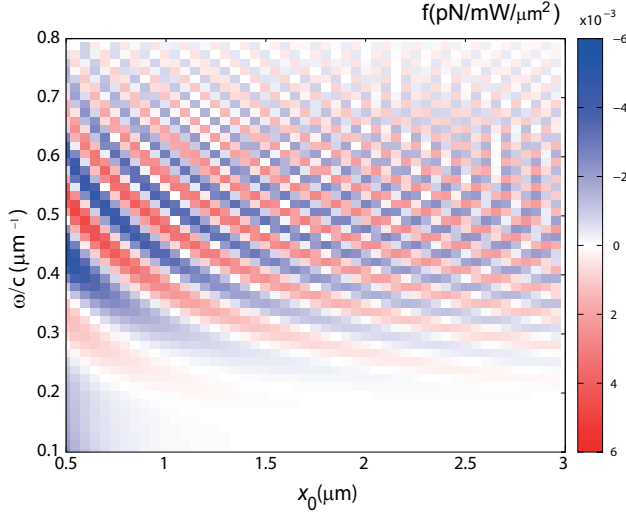


Figure 4: Map of the optical force as a function of the interparticle distance and frequency. All other parameters are the same as in Figure 2.

Next, we study the frequency dependence of the optical binding. Figure 4 shows a map of the optical force as a function of  $\omega/c$  frequency and the interparticle distance  $x_0$  for  $\mu_g = 0.3\text{eV}$ . For a fixed frequency value, we observe a periodic behaviour together with a decay of the oscillation amplitude with the  $x_0$  distance. This period decreases with frequency, which is in agreement with the fact that the GSP propagation constant, given by Eq. (E2), is an increasing function of frequency. It is worth noting that, although the force intensity decreases with the interparticle distance, the dependence with frequency is not like this. For a fixed  $x_0$  value, the force intensity increases until it reaches the maximum value at  $\approx 0.5\mu\text{m}^{-1}$  and then, the force intensity monotonously decreases with frequency. This behaviour can be understood from Eq. (16), where we can see that the force depends on the GSP propagation constant as  $F_x^{(x)}(x_0) \approx k_{sp}^4 Y_1(k_{sp}x_0)e^{-2k_{sp}z_0}$ . Then, for a fixed value of  $x_0$ , the function  $F_x^{(x)}$  reaches its maximum value for  $k_{sp} = 2/z_0 = 20\mu\text{m}^{-1}$ . From the dispersion relation plotted in Figure D.8 for  $\mu_g = 0.3\text{eV}$ , we find that the corresponding value for  $k_{sp}(\omega) = 20\mu\text{m}^{-1}$  is  $\omega/c = 0.52\mu\text{m}^{-1}$ , a value that agrees well with that numerically found. Even though for perpendicular polarization, the force presents a similar behaviour to that for parallel polarization shown in Figure 4, it is worth noting that, from Eq. (17), the frequency value where the force for perpendicular polarization reaches the maximum value verify the condition  $k_{sp}(\omega) = 3/(2z_0) = 15\mu\text{m}^{-1}$ , leading to  $\omega/c = 0.46\mu\text{m}^{-1}$ .

In order to study the optical binding dependence with graphene parameters, we calculate the interparticle force dependence with the chemical potential for normal incidence. Figure 5 shows the optical force as a function of the  $x_0$  distance and

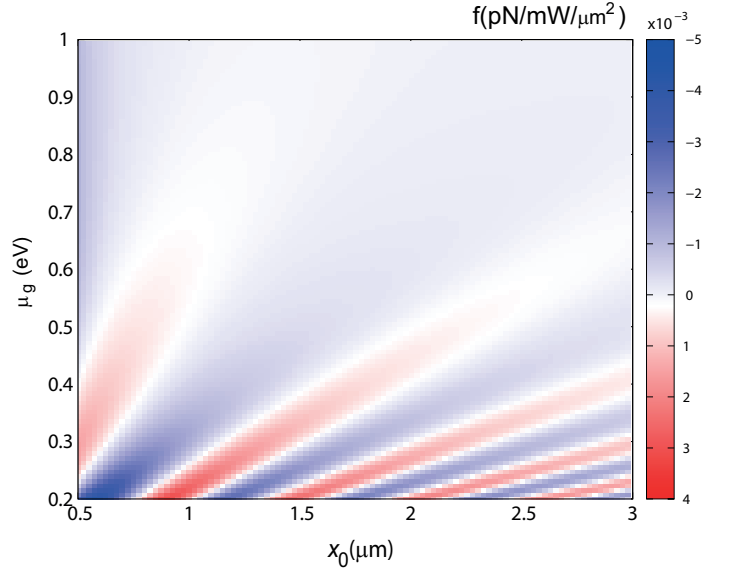


Figure 5: Map of the optical force as a function of the interparticle distance and chemical potential. All parameters are the same as in Figure 2.

the chemical potential. We observe zones for which the force is positive (red zones) and others where the force is negative (blue zones). Note that for a fixed chemical potential value, the force is a periodic function on the interparticle distance  $x_0$ , and that this period depends on the chemical potential value, being an increasing function of  $\mu_g$ . This can be understood from the quasistatic expression for the GSP propagation constant. From Eq. (E2), we see that  $k_{sp}$  is a decreasing function of  $\mu_g$ , thus the period of the function  $Y_1(k_{sp}x_0)$  in Eq. (16) and  $Y_2(k_{sp}x_0)$  in Eq. (17) increases with  $\mu_g$ . Unlike the case of surface plasmons on metallic materials, for which the plasmon kinematic quantities are fixed by an invariable charge density, GSPs provide a dynamic control on the optical binding period, and consequently, on the stable interparticle distance by varying the chemical potential of graphene.

Now, we investigate the optical binding properties under oblique incidence. We focus on the case in which the plane of incidence coincides with the  $x - z$  plane. Figure 6 shows the optical force, rigorously calculated, as a function of  $x_0$  for  $\theta_i = 10^\circ$  and  $30^\circ$ . The optical force on particle B for normal incidence is plotted as a reference. From Figure 6a we observe that the force on particle A is not opposite to the force on particle B, as in the case of normal incidence. This effect is essentially caused by two mechanisms. The first mechanism is associated with the incoming photon momentum parallel to the graphene surface: both particles are pushed in the  $+x$  direction, *i.e.*, in the direction of the incident photon propagation constant parallel to the graphene surface. The second mechanism is associated with the break of the mirror symmetry imposed by the oblique incidence, giving rise to different dipole moments induced on particles A and B and different forces on each of the particles take place. As a consequence, the equilibrium positions obtained for particle B (positions where the particle B is fixed) do not coincide with those obtained for par-

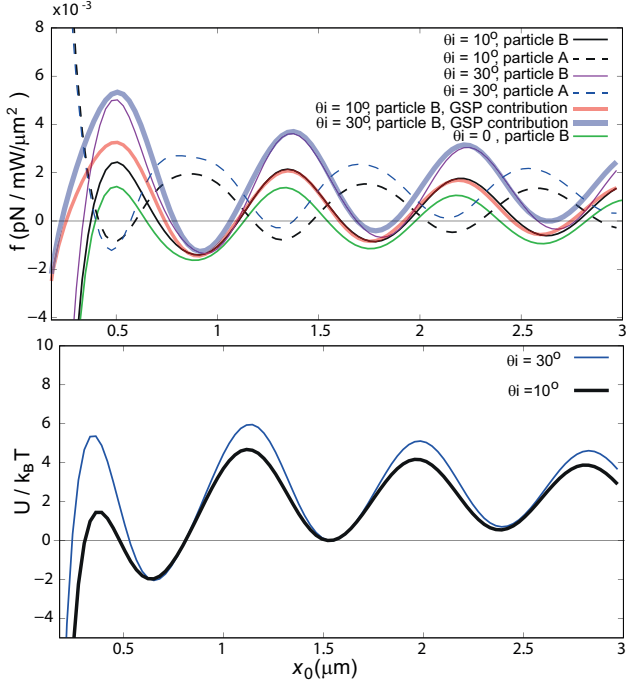


Figure 6: (a) Optical force and (b) potential energy of interaction between the particles A and B normalized to  $k_B T$ , as functions of the interparticle distance  $x_0$  for  $\omega/c = 0.325\mu\text{m}^{-1}$ . The incidence angles are  $\theta_i = 10^\circ, 30^\circ$ . The curve for normal incidence is given as a reference. The potential energy values have been calculated for an intensity  $I = 50\text{mW}/\mu\text{m}^2$ . All parameters are the same as in Figure 2.

ticle A. In addition, as  $\theta_i$  increases, the equilibrium positions are lost, as we can see for  $\theta_i = 30^\circ$ , where the particle A does not reach any equilibrium position for  $x_0 > 1.5\mu\text{m}$ . On the other hand, the potential energy of interaction between particles, *i.e.*, the potential referred to the relative positions between particles, reaches minimum values, as can be seen in Figure 6b where we have computed the potential for  $\theta_i = 10^\circ, 30^\circ$  and an intensity  $I = 50\text{mW}/\mu\text{m}^2$ . We recall that these positions do not correspond to stable equilibrium in which both particles are fixed, but to positions where the system attains internal equilibrium. A similar behaviour has been found for a dielectric interface in the total reflection configuration [3]. By using Eq. (18), we have calculated (Figure 6a) the GSP contribution to the optical force on particle B for  $\theta_i = 10^\circ$  and  $30^\circ$ . As in case of normal incidence, for an interparticle distance large enough, the plasmonic contribution follows well the behaviour of the optical force rigorously calculated by using Eq. (5).

Finally, we explore the influence of the shape of particles on the optical binding. To do this, cubic (with edge length  $a$  and cylindrical (with height  $h$  equal to diameter  $d$ ) shapes have been considered. The values of  $a$  and  $h$  have been chosen in such a way the volumes of the cubic, cylinder and sphere coincide. The quasistatic polarizabilities have been calculated using the formulas presented in [27].

From Figure 7 we see that the optical force curve for the case of two cylinders placed with the cross section along  $x-z$  plane (cylinders along  $y$  axis) matches with that correspond-

ing to spherical particles. This is to be expected because the value of the polarizability along an axis contained in the cylinder cross section almost coincides with that of the sphere of the same volume for  $\epsilon_p = 3.9$  [27]. When the cylinders are

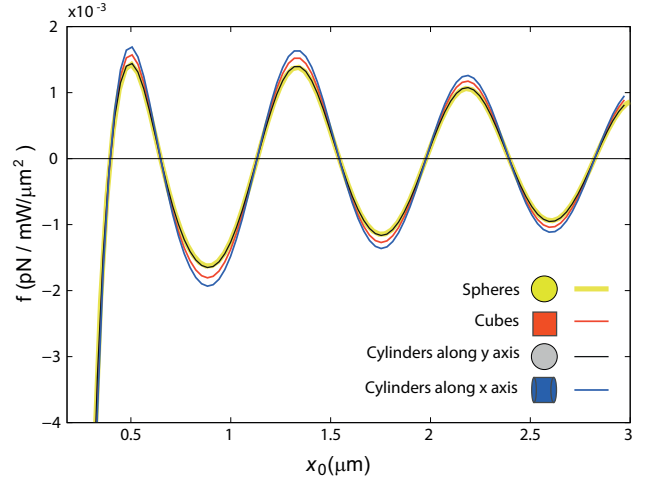


Figure 7: Optical force as a function of the interparticle distance  $x_0$  for normal incidence and various shapes. The radius of the sphere is  $R = 90\text{nm}$  and the volume of cubes and cylinders are equal to that of the sphere. All other parameters are the same as in Figure 2.

placed with their symmetry axis along the incident electric field direction (cylinders along  $x$  axis), the force amplitude increases as a consequence of the polarizability increment along this direction. On the other hand, the force curve for a cubic shape falls between the curves corresponding to spheres and cylinders aligned along the  $x$  axis.

#### 4. Conclusions

In conclusion, we have analyzed the benefits of a graphene sheet as a nanoparticle binder. Due to super confinement of GSPs, we found equilibrium interparticle distances of few micrometers for low frequency plane wave incidence, THz and IR. Moreover, these equilibrium distances can be dynamically controlled by chemical potential variations, a fact that highlights the use of graphene for optical binding applications.

In addition, using the dispersion properties of surface plasmons on a perfectly flat and infinite graphene sheet, we have obtained an analytical expression for the binding force that quantitatively explains the main results obtained by applying the rigorous Green's method.

The possibility to incorporate another graphene sheet forming a graphene parallel waveguide [31] or by creating a space layer forming an attenuated total reflection structure [32], allows interesting degree of freedoms to increase the GSP field and, as a consequence, the depth of the potential well of the optical force between particles. Although we are planning to report the results of such studies in future papers, as a first step, here we have restricted ourselves to performing an analysis of the optical binding properties on a single graphene sheet. In this way, we believe that our results are valuable in the framework of optical binding including graphene plasmonic structures.

## Acknowledgment

The authors acknowledge the financial supports of Universidad Austral O04-INV00020 and Consejo Nacional de Investigaciones Científicas y Técnicas (CONICET).

## Appendix A. Graphene conductivity

We consider the graphene layer as an infinitesimally thin, local and isotropic two-sided layer with frequency-dependent surface conductivity  $\sigma(\omega)$  given by the Kubo formula [28], which can be read as  $\sigma_{loc} = \sigma^{intra} + \sigma^{inter}$ , with the intraband and interband contributions being

$$\sigma^{intra}(\omega) = \frac{2ie^2k_B T}{\pi\hbar^2(\omega + i\gamma_g)} \ln \left[ 2 \cosh(\mu_g/2k_B T) \right], \quad (A1)$$

$$\sigma^{inter}(\omega) = \frac{e^2}{\hbar} \left\{ \frac{1}{2} + \frac{1}{\pi} \arctan \left[ \frac{(\hbar\omega - 2\mu_g)/2k_B T}{\gamma_g} \right] - \frac{i}{2\pi} \ln \left[ \frac{(\hbar\omega + 2\mu_g)^2}{(\hbar\omega - 2\mu_g)^2 + (2k_B T)^2} \right] \right\}, \quad (A2)$$

where  $\mu_g$  is the chemical potential (controlled with the help of a gate voltage),  $\gamma_g$  the carriers scattering rate,  $e$  the electron charge,  $k_B$  the Boltzmann constant and  $\hbar$  the reduced Planck constant. For chemical potential values substantially larger than the thermal energy, *i.e.*,  $k_B T \ll \mu_g$ , the graphene conductivity can be well approached by the intraband term which takes the Drude form,

$$\sigma(\omega) = \frac{ie^2\mu_g}{\pi\hbar^2(\omega + i\gamma_g)}. \quad (A3)$$

## Appendix B. Green tensor

The Green tensor  $\hat{\mathbf{G}}(\mathbf{r}, \mathbf{r}')$  is defined by the electric field at point  $\mathbf{r}$  generated by an electric dipole  $\mathbf{p}$  located at the source point  $\mathbf{r}'$  and satisfies [29],

$$\nabla \times \nabla \times \hat{\mathbf{G}}(\mathbf{r}, \mathbf{r}') - k_0^2 \hat{\mathbf{G}}(\mathbf{r}, \mathbf{r}') = \mathbf{I} \delta(\mathbf{r} - \mathbf{r}'), \quad (B1)$$

where  $\mathbf{I}$  is the unit tensor. By applying the superposition method, the solution of Eq. (B1) can be expressed as a sum of two parts, one of them,  $\hat{\mathbf{G}}_0(\mathbf{r}, \mathbf{r}')$ , is associated to the primary dipole emission of the source and the other,  $\hat{\mathbf{G}}_s(\mathbf{r}, \mathbf{r}')$ , takes into account the field scattered on  $z = 0$  surface. For  $z, z' > 0$  (upper half space), the expression for these functions have the form [29]:

$$\hat{\mathbf{G}}_0(\mathbf{r}, \mathbf{r}') = \frac{e^{ik_0 d}}{4\pi d} \times \left\{ \left[ 1 + \frac{ik_0 d - 1}{k_0^2 d^2} \right] \mathbf{I} + \frac{3 - i3k_0 d - k_0^2 d^2}{3k_0^2 d^2} \hat{\mathbf{r}} \hat{\mathbf{r}} \right\}, \quad (B2)$$

where  $d = |\mathbf{r} - \mathbf{r}'|$ , and

$$\hat{\mathbf{G}}_s(\mathbf{r}, \mathbf{r}') = \frac{i}{8\pi^2} \int_0^\infty dk_{\parallel} \mathbf{f}(k_{\parallel}, \rho) e^{i\gamma^{(1)}(z+z')}, \quad (B3)$$

where  $k_{\parallel}$  is the wave vector parallel to the surface,  $\rho = \sqrt{d^2 - (z - z')^2}$ ,  $\gamma^{(j)} = \sqrt{k_0^2 \varepsilon_j - k_{\parallel}^2}$  ( $j = 1, 2$ ). The cartesian components of  $\mathbf{f}(k_{\parallel}, \rho)$  are:

$$\mathbf{f}_{xx}(k_{\parallel}, \rho) = 2\pi \times \left\{ \frac{k_{\parallel}}{\gamma^{(1)}} \left[ -\cos(2\theta) \frac{J_1(k_{\parallel}\rho)}{k_{\parallel}\rho} + \cos^2(\theta) J_0(k_{\parallel}\rho) \right] r_s(k_{\parallel}) + \frac{k_{\parallel}\gamma^{(1)}}{k_0^2} \left[ \cos(2\theta) \frac{J_1(k_{\parallel}\rho)}{k_{\parallel}\rho} - \cos^2(\theta) J_0(k_{\parallel}\rho) \right] r_p(k_{\parallel}) \right\}, \quad (B4)$$

$$\mathbf{f}_{yy}(k_{\parallel}, \rho) = 2\pi \times \left\{ \frac{k_{\parallel}}{\gamma^{(1)}} \left[ -\cos(2\theta) \frac{J_1(k_{\parallel}\rho)}{k_{\parallel}\rho} + \cos^2(\theta) J_0(k_{\parallel}\rho) \right] r_s(k_{\parallel}) - \frac{k_{\parallel}\gamma^{(1)}}{k_0^2} \left[ \cos(2\theta) \frac{J_1(k_{\parallel}\rho)}{k_{\parallel}\rho} + \sin^2(\theta) J_0(k_{\parallel}\rho) \right] r_p(k_{\parallel}) \right\}, \quad (B5)$$

$$\mathbf{f}_{zz}(k_{\parallel}, \rho) = 2\pi \frac{k_{\parallel}^3}{k_0^2 \gamma^{(1)}} J_0(k_{\parallel}\rho), \quad (B6)$$

$$\mathbf{f}_{xy}(k_{\parallel}, \rho) = \mathbf{f}_{yx}(k_{\parallel}, \rho) = \pi \left\{ \frac{k_{\parallel}}{\gamma^{(1)}} r_s(k_{\parallel}) + \frac{k_{\parallel}\gamma^{(1)}}{k_0^2} r_p(k_{\parallel}) \right\} J_2(k_{\parallel}\rho) \sin(2\theta), \quad (B7)$$

$$\mathbf{f}_{xz}(k_{\parallel}, \rho) = -\mathbf{f}_{zx}(k_{\parallel}, \rho) = -2\pi i \frac{k_{\parallel}^2}{k_0^2} J_1(k_{\parallel}\rho) r_p(k_{\parallel}) \cos(\theta), \quad (B8)$$

$$\mathbf{f}_{yz}(k_{\parallel}, \rho) = -\mathbf{f}_{zy}(k_{\parallel}, \rho) = -2\pi i \frac{k_{\parallel}^2}{k_0^2} J_1(k_{\parallel}\rho) r_p(k_{\parallel}) \sin(\theta), \quad (B9)$$

where  $\theta$  is the angle between the axis joining the particles and the  $x$  axis, and  $J_n(x)$  is the Bessel function of  $n$ th order. The complex amplitude

$$r_p = \frac{\frac{\gamma^{(1)}}{\varepsilon_1} - \frac{\gamma^{(2)}}{\varepsilon_2} + \frac{Z_0 \sigma}{k_0} \frac{\gamma^{(1)}}{\varepsilon_1} \frac{\gamma^{(2)}}{\varepsilon_2}}{\frac{\gamma^{(1)}}{\varepsilon_1} + \frac{\gamma^{(2)}}{\varepsilon_2} + \frac{Z_0 \sigma}{k_0} \frac{\gamma^{(1)}}{\varepsilon_1} \frac{\gamma^{(2)}}{\varepsilon_2}}, \quad (B10)$$

is the Fresnel reflection coefficient for  $p$  polarization (magnetic field parallel to the  $z = 0$  surface),  $Z_0 = \sqrt{\mu_0/\varepsilon_0}$  is the vacuum impedance, whereas

$$r_s = \frac{\gamma^{(1)} - \gamma^{(2)} - Z_0 k_0 \sigma}{\gamma^{(1)} + \gamma^{(2)} + Z_0 k_0 \sigma}, \quad (B11)$$

is the Fresnel reflection for  $s$  polarization (electric field parallel to the  $z = 0$  surface).

In the case in which the particles are along the  $x$  axis, at heights  $z = z' = z_0$  and separated one from the other a distance  $x_0$ , *i.e.*,  $\mathbf{r} = x_0 \hat{x} + z_0 \hat{z}$  and  $\mathbf{r}' = z_0 \hat{z}$ , we must take  $\theta = 0$  in expressions (B4) to (B9). Moreover, Eq. (B2) is written as,

$$\hat{\mathbf{G}}_0(\mathbf{r}, \mathbf{r}') = \frac{e^{ik_0 x_0}}{4\pi x_0} \times \left\{ \left[ 1 + \frac{ik_0 x_0 - 1}{k_0^2 x_0^2} \right] \mathbf{I} + \frac{3 - i3k_0 x_0 - k_0^2 x_0^2}{3k_0^2 x_0^2} \hat{x} \hat{x} \right\}. \quad (B12)$$



### Appendix C. Incident field and induced dipole moments

To obtain the induced dipole moments due to the incoming and scattered electric fields, we follow the same steps as in Ref. [9]. In this manner, the dipole moments are written as

$$\mathbf{p}_A = \hat{\alpha}_s[\mathbf{E}_0(\mathbf{x}_A) + \frac{k_0^2}{\epsilon_0}\hat{\mathbf{G}}(\mathbf{x}_A, \mathbf{x}_B)\mathbf{p}_B], \quad (\text{D1})$$

and

$$\mathbf{p}_B = \hat{\alpha}_s[\mathbf{E}_0(\mathbf{x}_B) + \frac{k_0^2}{\epsilon_0}\hat{\mathbf{G}}(\mathbf{x}_B, \mathbf{x}_A)\mathbf{p}_A], \quad (\text{D2})$$

for particles A and B respectively. The first term in Eq. (D1) (Eq. (D2)) represents the incident and reflected electric field,  $\mathbf{E}_0(\mathbf{r}) = \mathbf{E}_i(\mathbf{r}) + \mathbf{E}_r(\mathbf{r})$ , whereas the second term represents the field in particle A (B) which is scattered by particle B (A). Here,  $\hat{\alpha}_s$  is the particle polarizability that accounts the corrections due to the scattering with the surface,

$$\hat{\alpha}_s = \frac{\alpha_0}{\hat{\mathbf{I}} - \frac{k_0^2}{\epsilon_0}\alpha_0\hat{\mathbf{G}}_s(\mathbf{r}_j, \mathbf{r}_j)}, \quad (\text{D3})$$

where  $j = A, B$ . In Eqs. (D1) and (D2) we have taken into account that particles A and B are identical. By solving Eqs. (D1) and (D2), we obtain

$$\mathbf{p}_A = \hat{\alpha}_s \frac{\mathbf{E}_0(\mathbf{x}_A) + \frac{k_0^2}{\epsilon_0}\hat{\mathbf{G}}(\mathbf{x}_A, \mathbf{x}_B)\hat{\alpha}_s\mathbf{E}_0(\mathbf{x}_B)}{\hat{\mathbf{I}} - \frac{k_0^4}{\epsilon_0^2}\hat{\alpha}_s\hat{\mathbf{G}}(\mathbf{x}_A, \mathbf{x}_B)\hat{\alpha}_s\hat{\mathbf{G}}(\mathbf{x}_B, \mathbf{x}_A)}. \quad (\text{D4})$$

In case where the incidence is on the  $x-z$  plane and for  $p$  polarization (electric field on the incidence plane), the explicit form of the incident electric field  $\mathbf{E}_i(\mathbf{r}_j)$  ( $j = A, B$ ) is given by,

$$\begin{aligned} \mathbf{E}_i(\mathbf{r}_A) &= E_i[\cos\theta_i \cos\phi_i \hat{x} + \cos\theta_i \sin\phi_i \hat{y} + \sin\theta_i \hat{z}] e^{-ik_0 \cos\theta_i z_0}, \\ \mathbf{E}_i(\mathbf{r}_B) &= E_i[\cos\theta_i \cos\phi_i \hat{x} + \cos\theta_i \sin\phi_i \hat{y} + \sin\theta_i \hat{z}] e^{ik_0(\sin\theta_i x_0 - \cos\theta_i z_0)}, \end{aligned} \quad (\text{D5})$$

where  $E_i$  is the amplitude of the incident plane electric field. The explicit form of the reflected field  $\mathbf{E}_r(\mathbf{r}_j)$  ( $j = A, B$ ) can be obtained from Eq. (D5) using the reflection coefficients  $r_p(k_{\parallel})$  defined in Eqs. (B10).

In many cases, for normal incidence for example, the electric fields at both particle positions are equal, *i.e.*,  $\mathbf{E}_0(\mathbf{r}_A) = \mathbf{E}_0(\mathbf{r}_B)$ . In such cases, Eq. (D4) can be written as

$$\mathbf{p}_A = \hat{\alpha}_A \mathbf{E}_0, \quad (\text{D6})$$

where we have defined the effective polarizability for particle A as

$$\hat{\alpha}_A = \hat{\alpha}_s \frac{\hat{\mathbf{I}} + \frac{k_0^2}{\epsilon_0}\hat{\mathbf{G}}(\mathbf{x}_A, \mathbf{x}_B)\hat{\alpha}_s}{\hat{\mathbf{I}} - \frac{k_0^4}{\epsilon_0^2}\hat{\alpha}_s\hat{\mathbf{G}}(\mathbf{x}_A, \mathbf{x}_B)\hat{\alpha}_s\hat{\mathbf{G}}(\mathbf{x}_B, \mathbf{x}_A)}. \quad (\text{D7})$$

Expressions for the dipole moment and polarizability on particle B are obtained from Eq. (D4) and (D7), respectively, by interchanging A and B.

### Appendix D. Graphene plasmon dispersion Characteristics

To obtain the dispersion characteristics of GSPs, we equate to zero the denominator in Eq. (B10),

$$\frac{\gamma^{(1)}}{\epsilon_1} + \frac{\gamma^{(2)}}{\epsilon_2} + \frac{Z_0\sigma}{k_0} \frac{\gamma^{(1)}}{\epsilon_1} \frac{\gamma^{(2)}}{\epsilon_2} = 0, \quad (\text{E1})$$

and solve for  $k_{\parallel}$ . In the non-retarded regime,  $k_0 \ll k_{sp}$ , the wavenumber  $k_{sp}$  can be approximated by [30]

$$k_{sp} = ik_0 \frac{\epsilon_1 \epsilon_2}{Z_0 \sigma (\epsilon_1 + \epsilon_2)} = k_0 \frac{\epsilon_1 \epsilon_2 \pi \hbar^2}{Z_0 e^2 \mu_g (\epsilon_1 + \epsilon_2)} (\omega + i\gamma_g), \quad (\text{E2})$$

where in the last equality we have used Eq. (A3). Figure D.8 shows the dispersion curves obtained by solving Eq. (E1) and the non-retarded expression Eq. (E2) for various values of chemical potential,  $\mu_g = 0.3, 0.7 \text{ eV}$ . We observe that results from Eq. (E2) agree well with the values obtained by solving the full retarded dispersion equation (E1).

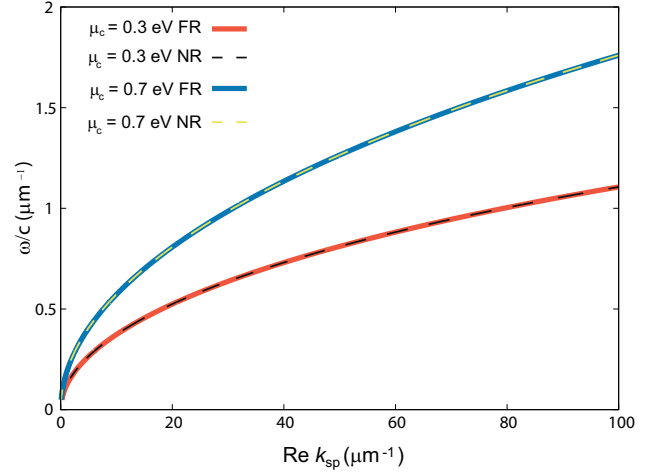


Figure D.8: GSP dispersion curves for  $\mu_g = 0.3, 0.7 \text{ eV}$ . Solid (dashed) line is obtained by using the full retarded (FR) Eq. (E1) (the non-retarded (NR) Eq. (E2)).

### Appendix E. Numerical method

The integration path in Eq. (6) is set along the real and positive  $k_{\parallel}$  axis, so that the integral will be strongly affected by singularities that are close to that axis. Pole singularities, zeroes of the denominator in  $r_p(k_{\parallel})$  coefficient, occur at complex location and it represents the propagation constant of the GSP mode. We transform the original oscillatory integrand function into one to avoid the complex singularities which lie near the real  $k_{\parallel}$  axis and then we apply a numerical quadrature to calculate the field integrals. To do this, we surround the pole singularity by deforming the integration path into the complex plane as shown in Figure E.9. The path I is an elliptical path starting at  $k_{\parallel} = 0$  with the major semi-axis  $k_{\parallel} = a$  and the minor semi-axis  $k_{\parallel} = b$ . In the region between path I and the real axis the integrand function is analytical, thus the Cauchy's

integral theorem implies that an integration on path I will be equal to the integral on the real axis from 0 to  $2a$ . The  $a$  value should be chosen large enough to surround the pole singularities, thus  $2a > k_{sp}$  must be fulfilled. In a first step we divide the integration interval into several subintervals and then apply the numerical quadrature in each subinterval. We have implemented a 32 point Gauss Legendre quadrature in each of such sub-interval.

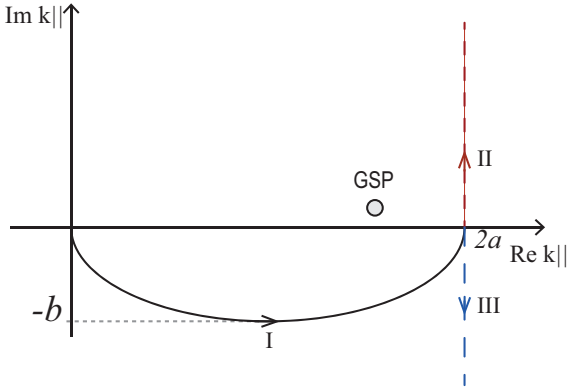


Figure E.9: Singularities and path of integration in the complex plane  $k_{||} = \text{Re } k_{||} + i\text{Im } k_{||}$  for the electromagnetic fields. The original path, along the positive semi-axis, is deformed along an elliptical path (I) surrounding the singularities, together with the paths (II) and (III) parallel to the imaginary  $k_{||}$  axis using Hankel functions.

Taking into account that,

$$J_n(z) = \frac{1}{2} [H_n^{(1)}(z) + H_n^{(2)}(z)], \quad (\text{E1})$$

and the fact that the Hankel functions of the first kind  $H_n^{(1)}(z)$  and the second kind  $H_n^{(2)}(z)$  decrease faster as long as  $|\text{Im } z|$  increases in the sector  $\text{Im } z > 0$  and  $\text{Im } z < 0$ , respectively, the remaining integration is carried out by deflecting the integration path from the real axis to a path parallel to the imaginary  $k_{||}$  axis as shown in Figure E.9, with  $\text{Im } k_{||} > 0$  for  $H_n^{(1)}(k_{||}\rho)$  (path II) and with  $\text{Im } k_{||} < 0$  for  $H_n^{(2)}(k_{||}\rho)$  (path III). In the region between path II and the real axis the integrand has no pole singularities, thus Cauchy's integral theorem implies that the integral on a closed path in this region will be zero. Therefore, the integral over path II in the direction shown in Figure E.9 is equal to that from  $2a$  to  $+\infty$  over the real axis. In a similar way, one can demonstrate that the integral over path III in the direction shown in Figure E.9 is equal to that from  $2a$  to  $+\infty$  over the real axis. In our implementation, we have used a 32 point Gauss Legendre quadrature to calculate the field integrals on paths I, II and III.

## References

- [1] K Dholakia, and P Zemanek, "Colloquium: Gripped by light: Optical binding," *Rev. Mod. Phys.* 82, (2010), 1767–1791.
- [2] K Forbes, DS Bradshaw, and DL Andrews, "Optical binding of nanoparticles," *Nanophotonics* 9, (2020), 1–17.

- [3] PC Chaumet, and M Nieto-Vesperinas, "Optical binding of particles with or without the presence of a flat dielectric surface," *Phys. Rev. B* 64, 035422 (2001).
- [4] Z Yan, RA Shah, G Chado, SK Gray, M Pelton, and NF Scherer, "Guiding Spatial Arrangements of Silver Nanoparticles by Optical Binding Interactions in Shaped Light Fields," *ACS Nano* 2013 7, (2013) 1790–1802.
- [5] MM Salary, and H Mosallaei, "Tailoring optical forces for nanoparticle manipulation on layered substrates," *Phys. Rev. B* 94, 035410 (2016).
- [6] V Demergis and E-L Florin, "Ultrastrong Optical Binding of Metallic Nanoparticles," *Nano Lett.* 12, (2012) 5756–5760
- [7] M. Siler, T. Cizmar, M. Sery, and P. Zemanek, "Optical forces generated by evanescent standing waves and their usage for sub-micron particle delivery" *Appl. Phys. B* 84, 157–165 (2006).
- [8] X. Hand, and P. H. Jones, "Evanescent wave optical binding forces on spherical microparticles," *Opt. Lett.* 40, 4042–4045 (2015)
- [9] N Kostina, M Petrov, A Ivinskaya, S Sukhov, A Bogdanov, I Toftul, M Nieto-Vesperinas, P Ginzburg, and A Shalin, "Optical binding via surface plasmon polariton interference," *Phys. Rev. B* 99, 125416 (2019).
- [10] NA Kostina, DA Kislov, AN Ivinskaya, A Proskurin, DN Redka, A Novitsky, P Ginzburg, and AS Shalin, "Nanoscale Tunable Optical Binding Mediated by Hyperbolic Metamaterials," *ACS Photonics* 7, (2020), 425–433.
- [11] A. Singh, M. Andrello, N. Thawdar, J. M. Jornet, "Design and operation of a graphene-based plasmonic nano-antenna array for communication in the terahertz band," *IEEE J. Sel. Areas Commun.* 38, 2104–2117 (2020).
- [12] R. Filter, M. Farhat, M. Steglich, R. Alaei, R. Rockstuhl and F. Lederer, "Tunable graphene antennas for selective enhancement of THz-emission," *Opt. Express*, 21 (2013), p. 3737, (2020).
- [13] J. Nong, L. Tang, G. Lan, P. Luo, Z. Li, D. Huang, J. Yi, H. Shi, W. Wei, "Enhanced Graphene Plasmonic Mode Energy for Highly Sensitive Molecular Fingerprint Retrieval," *Laser Photonics Rev.* 15, 2000300 (2021)
- [14] L. Prelat, M. Cuevas, N. Passarelli, R. Bustos Marún, and R. Depine, "Spaser and optical amplification conditions in graphene-coated active wires," *J. Opt. Soc. Am. B* 38, 2118–2126 (2021)
- [15] D. T. Debu, F. T. Ladani, D. French, S. J. Bauman and J. B. Herzog, "Hyperbolic plasmon-phonon dispersion on group velocity reversal and tunable spontaneous emission in graphene-ferroelectric substrate," *Npj 2D Mater. Appl.* 3, 1 (2019).
- [16] J. Olivo, M. Cuevas, "Enhanced energy transfer via graphene-coated wire surface plasmons," *J. Quant. Spectrosc. Radiat. Transfer* 239, (2019) 106655.
- [17] G. A. Jones, D. S. Bradshaw, "Resonance Energy Transfer: From Fundamental Theory to Recent Applications," *Front. Phys.* 7, (2019)
- [18] D. O. Herasymova, S. V. Dukhopelnykov, and A. I. Nosich, "Infrared diffraction radiation from twin circular dielectric rods covered with graphene: plasmon resonances and beam position sensing," *J. Opt. Soc. Am. B* 38, C183-C190 (2021).
- [19] A. V. Maslov, "Optical equilibrium for resonant particles induced by surface plasmons of two-dimensional materials," *Phys. Rev. B* 98, 235414 (2018)
- [20] P. Q. Liu and P. Paul, "Graphene Nanoribbon Plasmonic Conveyor Belt Network for Optical Trapping and Transportation of Nanoparticles," *ACS Photonics* 7, (2020) 3456–3466
- [21] Zi Shen, M. Becton, D. Han, X. Fang, X. Wang, L. Zhang, and X. Chen, "Terahertz plasmonic nanotrapping with graphene coaxial apertures," *Phys. Rev. A* 102, 053507 (2020).
- [22] M. Samadi, S. Darbari and M. K. Moravvej-Farshi, "Numerical Investigation of Tunable Plasmonic Tweezers based on Graphene Stripes," *Sci. Rep.* 7 14533 (2017)
- [23] A. F. da Mota, A. Martins, J. Weiner, P. Courteille, E. R. Martins, and B. V. Borges, "Design and analysis of nanopatterned graphene-based structures for trapping applications," *Phys. Rev. B* 102, 085415 (2020)
- [24] H. Chen, Y. Huang, "Tunable optical force on nonlinear graphene-wrapped nanoparticles," *Phys. Lett. A* 384 (2020) 126733
- [25] J Olivo, CJ Zapata-Rodríguez, M Cuevas, "Spatial modulation of the electromagnetic energy transfer by excitation of graphene waveguide surface plasmons," *J. Opt.* 21, 045002 (2019).
- [26] P. C. Chaumet and M. Nieto-Vesperinas, "Time-averaged total force on a dipolar sphere in an electromagnetic field," *Opt. Lett.* 25, 1065–1067 (2000).

[27] A Sihvola, J Venermo, and P Ylä-Oijala, Dielectric response of matter with cubic, circular-cylindrical, and spherical microstructures, *Mic and Opt Tech Lett* 41, (2004).

[28] Mikhailov SA and Sieglar K New electromagnetic mode in graphene *Phys. Rev. Lett.* 99, 016803 (2007)

[29] Novotny L, and Hecht B *Principles of Nano-Optics*; Cambridge University Press: New York, 2006.

[30] M. Jablan, H. Buljan, M. Soljagic "Plasmonics in graphene at infrared frequencies," *Phys. Rev. B*, 80 (24) (2009), p. 245435

[31] M Cuevas, Surface plasmon enhancement of spontaneous emission in graphene waveguides, *J. Opt.* 18 105003, (2016).

[32] M Cuevas, Critical coupling of surface plasmons in graphene attenuated total reflection geometry, *Phys. Lett. A*, 380 (2016), 4027-4031